

# On the interactions between strain accumulation, microstructure, and fatigue crack behavior

Jay D. Carroll · Wael Z. Abuzaid ·  
John Lambros · Huseyin Sehitoglu

Received: 18 October 2012 / Accepted: 28 January 2013 / Published online: 26 February 2013  
© Springer Science+Business Media (outside the USA) 2013

**Abstract** Fatigue crack growth is a complex process that involves interactions between many elements ranging across several length scales. This work provides an in-depth, experimental study of fatigue crack growth and the relationships between four of these elements: strain field, microstructure, crack path, and crack growth rate. Multiple data sets were acquired for fatigue crack growth in a nickel-based superalloy, Hastelloy X. Electron backscatter diffraction was used to acquire microstructural information, scanning electron microscopy was used to identify locations of slip bands and crack path, and optical microscopy was used to measure crack growth rates and to acquire images

for multiscale digital image correlation (DIC). Plastic strain accumulation associated with fatigue crack growth was measured at the grain level using DIC. An ex situ technique provided sub-grain level resolution to measure strain variations within individual grains while an in situ technique over the same regions showed the evolution of strain with crack propagation. All of these data sets were spatially aligned to allow direct, full-field comparisons among the variables. This in-depth analysis of fatigue crack behavior elucidates several relationships among the four elements mentioned above. Near the crack tip, lobes of elevated strain propagated with the crack tip plastic zone. Behind the crack tip, in the plastic wake, significant inhomogeneities were observed and related to grain geometry and orientation. Grain structure was shown to affect the crack path and the crack growth rate locally, although the global crack growth rate was relatively constant as predicted by the Paris law for loading with a constant stress intensity factor. Some dependency of crack growth rate on local strain and crack path was also found. The experimental comparisons of grain structure, strain field, and crack growth behavior shown in this work provide insight into the fatigue crack growth process at the sub-grain and multi-grain scale.

**Electronic supplementary material** The online version of this article (doi:10.1007/s10704-013-9813-8) contains supplementary material, which is available to authorized users.

J. D. Carroll (✉)  
Sandia National Laboratories, PO Box 5800,  
Albuquerque, NM 87185-0889, USA  
e-mail:jcarrol@sandia.gov

W. Z. Abuzaid · H. Sehitoglu  
Mechanical Science and Engineering,  
University of Illinois at Urbana-Champaign,  
160 Mechanical Engineering Building,  
1206 W. Green St., Urbana, IL 61801, USA

J. Lambros  
Aerospace Engineering, University of Illinois at  
Urbana-Champaign, 306 Talbot Laboratory,  
104 S. Wright St., Urbana, IL 61801, USA

**Keywords** Microstructure · Strain · Digital image correlation · Fatigue crack propagation · Plasticity · Experimental

## 1 Introduction

Fatigue crack growth measurements have been undertaken by many researchers at the macroscale (averaged over many grains) and engineering relationships between applied load, crack length, and fatigue crack growth rates have been published widely. However, it is known that the fatigue crack growth process also involves a number of interacting variables such as crack path, microstructure, and local strain fields. Some fatigue crack growth situations can involve even more variables such as strain rate, creep, corrosion, temperature, and microstructural changes. To complicate the situation further, a two-way coupling exists between some variables (e.g., strain field and crack path, temperature and stress, crack growth rate and corrosion). The specifics of the interactions between these variables determines the overall crack growth behavior. This work focuses on four of the most prominent and common parameters in fatigue crack growth (crack path, microstructure, crack growth rate, and strain field), and elucidates some of the relationships among them.

Several researchers have worked on clarifying the relationships between the many parameters influencing fatigue crack growth. Most notably, the Paris relationship (McEvily and Boettner 1963; Paris and Erdogan 1963) relates crack growth rate to material properties (inherent to the microstructure) and far-field loading. The discovery of crack closure (Elber 1970, 1971) revealed a dependency of crack growth rate on the strain field (plasticity induced closure), crack path (roughness induced closure), environment (oxidation induced closure), and microstructure (transformation induced crack closure) (Suresh and Ritchie 1984). Although the phenomenon of crack closure involves relationships among many of the relevant variables, its inclusion does not provide a fully predictive model as these are not the only relationships that exist between these variables. One effect of microstructure on crack path was elucidated by Forsyth (1963), who identified stage I crack growth, where the crack path is strongly dependent on local microstructure, and stage II crack growth, where the crack path is primarily determined by the far-field loading conditions. Work by Laird (1967) and many other researchers (e.g., Laird and Smith 1963; McEvily and Johnston 1967; Davidson 1984; Tanaka et al. 1984; Lankford 1985; Peralta and Laird 1998; Ritchie 1999) revealed several other relationships between relevant variables in fatigue crack growth such as the

micromechanisms of fatigue crack growth. However, work in this field continues because firm, quantitative relationships between most variables remain elusive.

In particular, the relationship between the strain field and other fatigue crack parameters remains unclear. Investigating these relationships has been a topic of research for decades. Some early research consisted of measurements at a few selected locations (Elber 1971; Liu and Ke 1975; Nicoletto et al. 1982; Sharpe Jr 1982). Full-field measurements of the strain fields around cracks subsequently became available through the use of a number of optical techniques including: moiré interferometry (Kobayashi et al. 1967; Liu and Ke 1975; Sanford and Dally 1979; Barker et al. 1985; Sanford 1989; Kmiec 1994), holography (Sanford 1989), photoelasticity (to measure stress fields) (Eftis et al. 1977; Sanford 1989), stereovision (a precursor to digital image correlation—DIC) (Williams et al. 1980; Gerberich et al. 1990), and DIC (McNeill et al. 1987; Luo et al. 1993; Carroll et al. 2009). However, most of these studies examined a single load cycle for the purpose of extracting fracture mechanics parameters. Few measurements of full-field strain accumulation over a number of fatigue crack growth cycles have been made, (Gerberich et al. 1990; Carroll et al. 2012a).

Because it has no inherent length scale, the advent of DIC (and the closely-related grid technique) opened up the possibility of relating full-field strain measurements at the grain level to microstructure (Delaire et al. 2000; Zhang and Tong 2004; Hériprié et al. 2007; Peralta et al. 2007; Zhao et al. 2008; El Bartali et al. 2009; Roux et al. 2009; Tschopp et al. 2009; Carroll et al. 2010, 2012a,b; Merzouki et al. 2010; Rehrl et al. 2011; Littlewood and Wilkinson 2012; Padilla et al. 2012). The majority of grain level DIC studies only consider uniaxial tension loading, but some examine the development of grain-level strains in fatigue (Tschopp et al. 2009; Efstathiou et al. 2010; Littlewood and Wilkinson 2012). However, few studies measure strains associated with fatigue crack growth at the grain level (Li and Orlecky 1993; Peralta et al. 2007; Carroll et al. 2012a).

Although several global relationships between the aforementioned variables are known, such as those stated in the second paragraph of the introduction, the local and multiscale (i.e., spanning from the microstructure to the macroscale) relationships between these variables is not well understood. The present work expands on the understanding of these

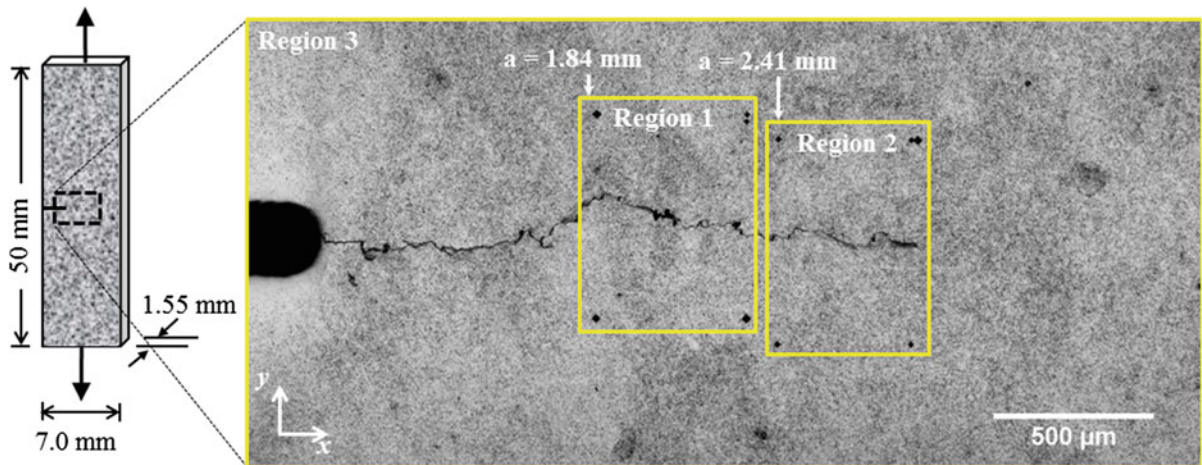


**Fig. 1** Specimen dimensions and regions of interest. This speckle pattern was suitable for all three levels of DIC resolution throughout these three regions of interest. Crack lengths at the start of regions 1 and 2 are indicated

local relationships by providing very high resolution, both spatially and temporally, experimental measurements of these parameters aligned with one another and directly comparing them. In this work, we combine elements from many of the aforementioned studies to investigate the relationships between crack path, microstructure, crack growth rate, and strain field in fatigue crack growth. High resolution DIC measurements of strain accumulation in fatigue crack growth are obtained, and these plastic strains are related to grain structure measured by electron backscatter diffraction (EBSD). In contrast with most previous studies, the DIC measurements shown in this work are measures of *plastic* strain accumulation over a number of cycles of fatigue crack growth (elastic strains are not included). Consequently, this study is one of the first to relate measurements of full-field strain *accumulation* to grain structure. In situ DIC measurements in a servohydraulic load frame show the development of grain-level strain fields over time, and sub-grain level measurements of strain accumulation in the same regions are made using a high resolution, *ex situ* DIC technique. Additionally, crack path and crack growth rate are examined in relation to these microstructure and strain measurements.

## 2 Methods

The material studied in this work is Hastelloy X, a nickel-based superalloy with the following pertinent

material properties: yield strength = 348 MPa, ultimate strength = 730 MPa, ductility = 54 %, elastic modulus = 205 GPa, Poisson's ratio = 0.32 (Haynes International, Inc.). A single edge notch tension specimen with dimensions  $50 \times 7.0 \times 1.55$  mm and a 0.99 mm notch (Fig. 1) was machined using electrical discharge machining. The specimen was polished with increasingly fine silicon carbide polishing powders down to  $0.05 \mu\text{m}$  followed by vibratory polishing with  $0.05 \mu\text{m}$  colloidal silica to produce a surface finish suitable for EBSD.

Material deformation associated with fatigue crack growth was studied in three regions of the specimen as shown in Fig. 1. Region 3 comprises an area that includes the entire crack line from the notch tip to the final crack tip position (approximately 2.0 mm wide by 1.0 mm tall). DIC measurements of full-field strain accumulation were made throughout this region after the last load cycle (cycle number 208,434) was applied to the specimen (using a DIC reference image captured before fatigue loading). Regions 1 and 2, the smaller regions in Fig. 1, measure  $630 \times 470 \mu\text{m}$  and  $630 \times 410 \mu\text{m}$ , respectively. The crack length, as it entered regions 1 and 2, was 1.84 and 2.41 mm as annotated in Fig. 1. These two smaller regions were studied in greater detail as the crack passed through each region. The full-field strain accumulation within each region was measured, *in situ*, every 64 cycles by DIC (using commercially available software, Vic2d, from Correlated Solutions, Inc.). This was accomplished by correlating minimum-load images captured at the

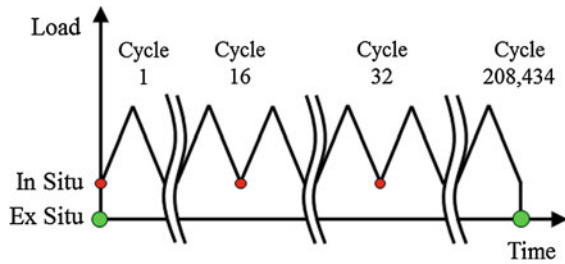


**Fig. 2** Image capture times with respect to fatigue loading. In situ DIC images were captured every 16 cycles at minimum load. Ex situ DIC images of the unloaded specimen were only captured before and after fatigue loading

measurement cycle to the reference image captured before fatigue loading, as illustrated in Fig. 2. After the crack had grown through regions 1 and 2, cycling was stopped, the specimen was unloaded, and high resolution, full-field DIC measurements of strain accumulation between the initial and final states, green markers in Fig. 2, were obtained using the techniques described in (Carroll et al. 2010).

Two microscopes were used to capture images for this experiment. A microscope mounted on a 3-axis stage near the load frame was used to acquire in situ images of regions 1 and 2 every 16 cycles (red markers in Fig. 2). The major advantage of this in situ optical microscope setup is that it allows a large number of cycles to be accumulated through the use of a servohydraulic load frame (in contrast to using a screw-driven in situ load frame in a scanning electron microscope). A 10 $\times$  magnification objective was used to obtain an image scale of 0.43  $\mu\text{m}/\text{pix}$  (corresponding to an image size of 688  $\times$  516  $\mu\text{m}$ ). A separate microscope was used for ex situ imaging of the unloaded specimen before and after fatigue loading. High resolution DIC results for regions 1 and 2 were obtained by stitching 36 images (per region) at a scale of 0.087  $\mu\text{m}/\text{pix}$  (50 $\times$  magnification with an image size of 139  $\times$  104  $\mu\text{m}$ ). Ex situ imaging of region 3 was performed at a scale of 0.87  $\mu\text{m}/\text{pix}$  (5 $\times$  magnification with an image width of 1.39  $\times$  1.04 mm) using a montage of three images.

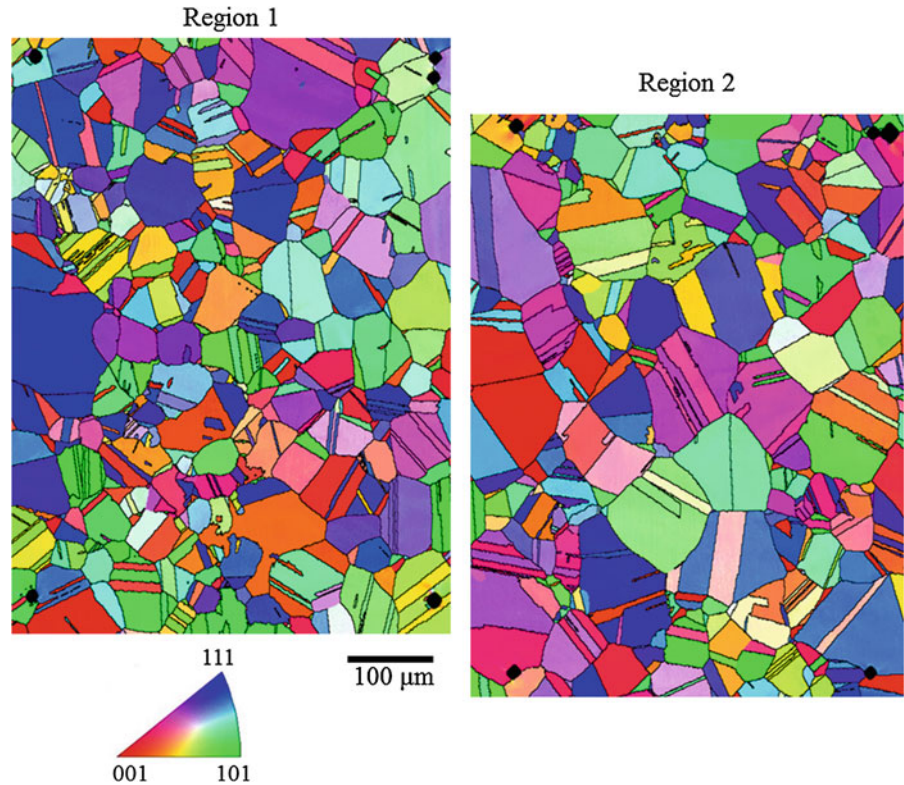
Although images were captured every 16 cycles, DIC was performed on the in situ images in regions 1 and 2 at intervals of 64 cycles to reduce the computational load. The speckle pattern allowed a subset size of 9  $\times$  9  $\mu\text{m}$  (21  $\times$  21 pix) and a subset spacing of 2.2  $\mu\text{m}$  (5 pix) to be used. As a result, full-field DIC measurements of the strain field were obtained for roughly 1,200

measurement cycles as the crack grew across the region 1. Similarly, strain fields for 900 measurement cycles were obtained for region 2. These measurements show the evolution of the strain field with crack growth, and its relationship to grain structure. Using ex situ images, high resolution DIC was performed throughout regions 1 and 2 using a subset size of 7  $\times$  7  $\mu\text{m}$  (81  $\times$  81 pix) and a subset spacing of 0.9  $\mu\text{m}$  (10 pix). These high resolution measurements allow the strains inside grains and across multiple grains to be visualized. The DIC results for region 3 were calculated using a subset size of 27  $\times$  27  $\mu\text{m}$  (31  $\times$  31 pix) and a subset spacing of 4.4  $\mu\text{m}$  (5 pix). The measurements throughout this region provide a larger view of the strain field surrounding regions 1 and 2.

Before loading the specimen, microstructural measurements were acquired throughout regions 1 and 2 using EBSD. Grain orientation maps of these two regions are shown in Fig. 3; each map is a compilation of four EBSD scans. The five Vickers indentation markers in the corners of each map, and at corresponding locations in Fig. 1, were used as fiducial markers to spatially overlay DIC strain measurements (both in situ and ex situ) with EBSD measurements of microstructure. After EBSD was performed, a speckle pattern was applied to the specimen by depositing 1  $\mu\text{m}$  silicon powder on the surface. This speckle pattern, visible in Fig. 1, was suitable for all three levels of DIC resolution.

Fatigue loading was applied at a rate of 1 Hz. The crack initiated at the notch tip after 9,000 cycles and grew until entering region 1 around cycle 72,000. As the crack grew across the first region of interest, the change in stress intensity factor,  $\Delta K$ , was held constant at 18.3  $\pm$  0.3  $\text{MPa}\sqrt{\text{m}}$  by load shedding. The crack finished growing through region 1 around cycle 149,000, spending a total of 77,000 cycles within the region. The crack entered region 2 around cycle 166,000 and grew through the region for 42,000 cycles until exiting around cycle 208,000. While the crack tip was within the second region of interest, the fatigue loading was held at a constant load amplitude so that  $\Delta K$  increased from 18.2 to 22.7  $\text{MPa}\sqrt{\text{m}}$  (at 1 Hz) as the crack length increased. The minimum load was held constant at 0.2 kN throughout the entire fatigue loading so that the loading ratio,  $R$ , rose from 0.07 to 0.14 throughout the test. The difference in load amplitude between regions 1 and 2 did not appear to have a significant effect except in long-term crack growth rates.

**Fig. 3** Grain orientation maps for regions 1 and 2. The color corresponds to the orientation of the grain in relation to the loading axis



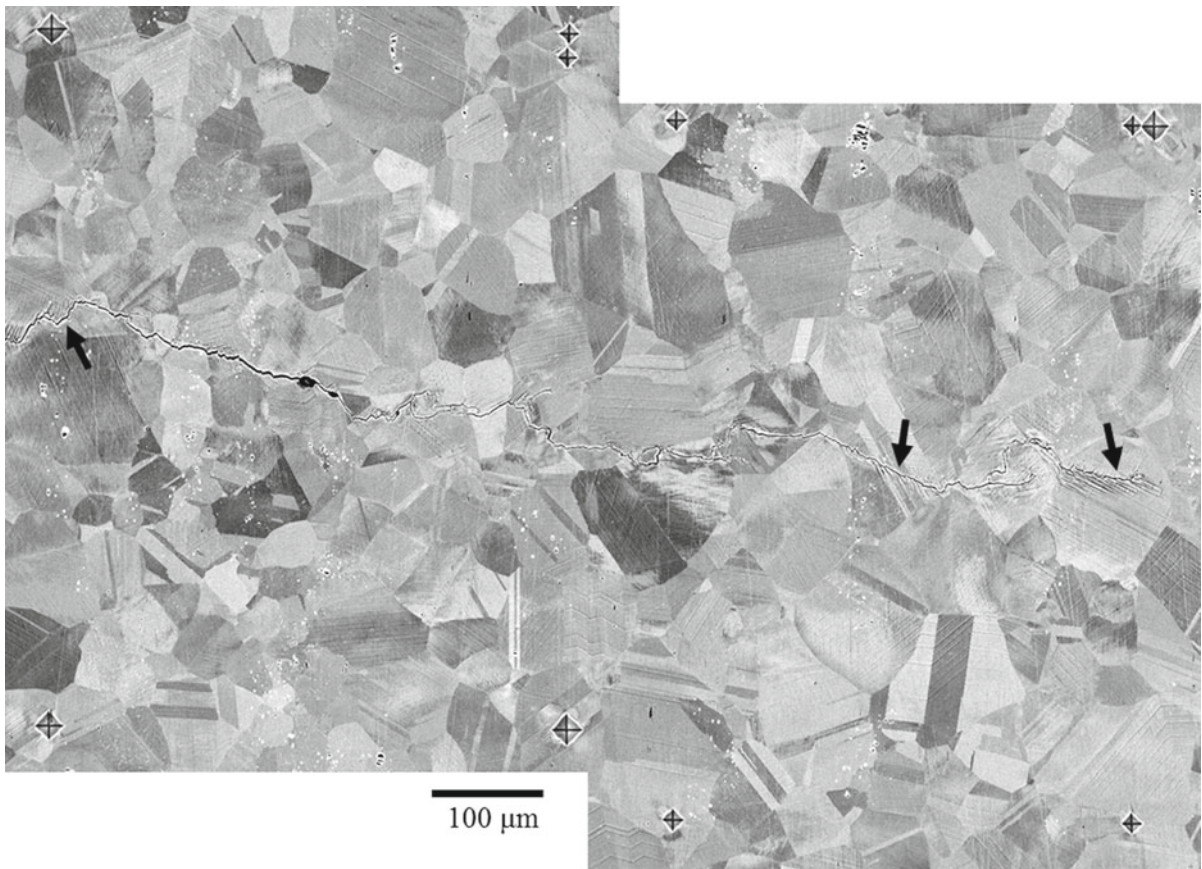
After the crack had grown through regions 1 and 2, fatigue loading was stopped and the specimen was imaged in the scanning electron microscope. A backscatter electron image of regions 1 and 2 after fatigue loading is shown in Fig. 4. This image shows the crack path, and grain geometry near the crack. Furthermore, slip bands generated by the growing fatigue crack are visible. Some slip bands develop in grains that are relatively far from the crack path. Other slip bands develop on the crack flanks and appear to influence crack path and crack growth rate (discussed later). These crack-flank slip bands are indicated by arrows in Fig. 4.

### 3 Results

The strain throughout region 3, which accumulates over the entire period of fatigue crack initiation and growth (208,434 cycles), is plotted in Fig. 5. In essence, this is a quantitative measure of the plastic wake produced during fatigue crack growth. This figure shows the strain field component perpendicular to the crack,  $\varepsilon_{yy}$ . The

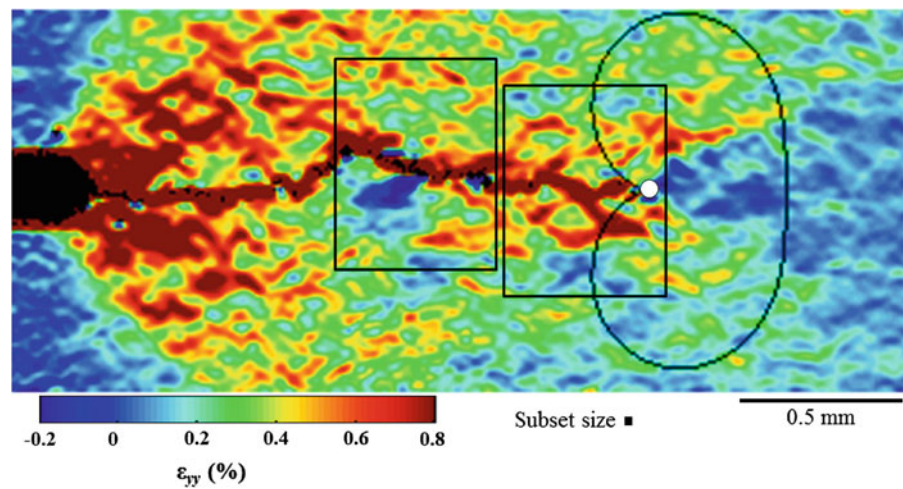
starter notch tip is shown in black at the left edge of the plot, the final crack tip position is highlighted by a white circle, and the subset size is shown below the plot as an estimate of the spatial resolution of these measurements. As the crack grew, the material on the crack flanks separated so that the DIC algorithm detected a strain along the crack line; consequently, the crack path is apparent from the high measured strain levels associated with it. This path is also verified by comparison with the image of Fig. 4.

The strain field in Fig. 5 exhibits two high-strain lobes that emanate from the final crack tip position such that the material directly ahead of the crack tip is relatively unstrained. The strain field also displays a considerable amount of inhomogeneity with some regions straining by over 1% strain and others experiencing a slight compressive plastic strain (including one region with a compressive strain on the order of  $-1\%$ ). These inhomogeneities are not noise in the DIC results since the strain resolution of these measurements is around 0.1% strain. Plastic strain is observed throughout the entire height of region 3, dropping off near the top and bottom edges. This indicates that the field of view



**Fig. 4** Backscatter electron image of regions 1 and 2 after the fatigue crack had grown through both regions. Several locations (indicated by *arrows*) along the crack path show *slip lines* emanating from the crack path into the grains containing the crack

**Fig. 5** Strain accumulation throughout region 3 over a period of 208,434 cycles. Strain is perpendicular to the crack,  $\epsilon_{yy}$ . The plane stress Von Mises estimate of the plastic zone is drawn in *black*. The locations of regions 1 and 2 are illustrated by *black rectangles*



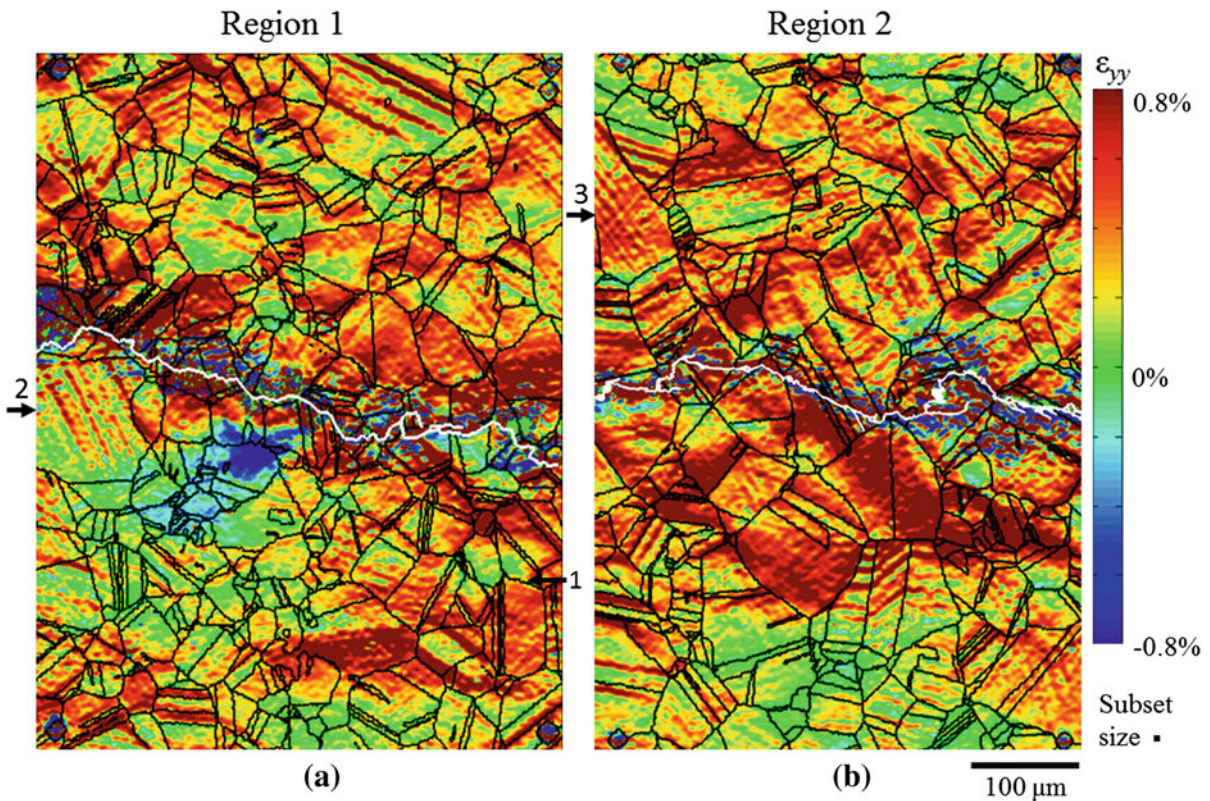


**Fig. 6** High resolution strain field,  $\varepsilon_{yy}$  (strain perpendicular to the *crack line*), throughout **a** region 1 and **b** region 2. Grain boundaries are overlaid in *black*, and the crack path is drawn in *white*

provided by region 3 is approximately the same height as the plastic wake throughout crack growth (with the exception of the notch-tip plastic region, which is naturally larger). The plane stress Von Mises estimate of the plastic zone is drawn in black in Fig. 5 (estimated for a stress intensity factor,  $K$ , of  $20.5 \text{ MPa}\sqrt{\text{m}}$  and a yield stress of  $385 \text{ MPa}$ ), and has a height of roughly  $1.1 \text{ mm}$ . The locations of regions 1 and 2 are illustrated by black rectangles. Clearly these two regions are well within this plastic zone of the propagating crack tip.

Plots of the high resolution strain fields,  $\varepsilon_{yy}$ , throughout regions 1 and 2 are shown in Fig. 6. The crack path is illustrated in white and grain boundaries from EBSD are shown in black. The subset size, an estimate of the spatial resolution of DIC measurements, is shown at the bottom right. These plots show a considerable amount of inhomogeneity at the grain and subgrain levels. On the scale of multiple grains, there is considerable variation in average strain levels from one grain to another (as indicated at point number 1

in Fig. 6). In some locations, significant strain accumulation occurs within a grain near the grain boundary while the neighboring grain exhibits relatively little strain near the same grain boundary (number 1). This indicates a grain boundary that has blocked dislocation motion between grains. While some grains accumulate more strain than others, there are very few grains in which the strain is homogeneous. Much of the strain variation within grains is in the form of slip bands within grains (number 2). A few locations also show evidence of multiple active slip systems within a single grain indicated by lines of strain localizations at multiple angles (point 3).

The strain plots in Fig. 6 show the final strain accumulation field after crack growth has finished (i.e., after cycle 208,434), but they contain little information on how those strain fields developed. The in situ strain fields that were captured every 64 cycles are better suited to provide information on the change in strain fields with time. Six of these  $\varepsilon_{yy}$  strain fields are shown

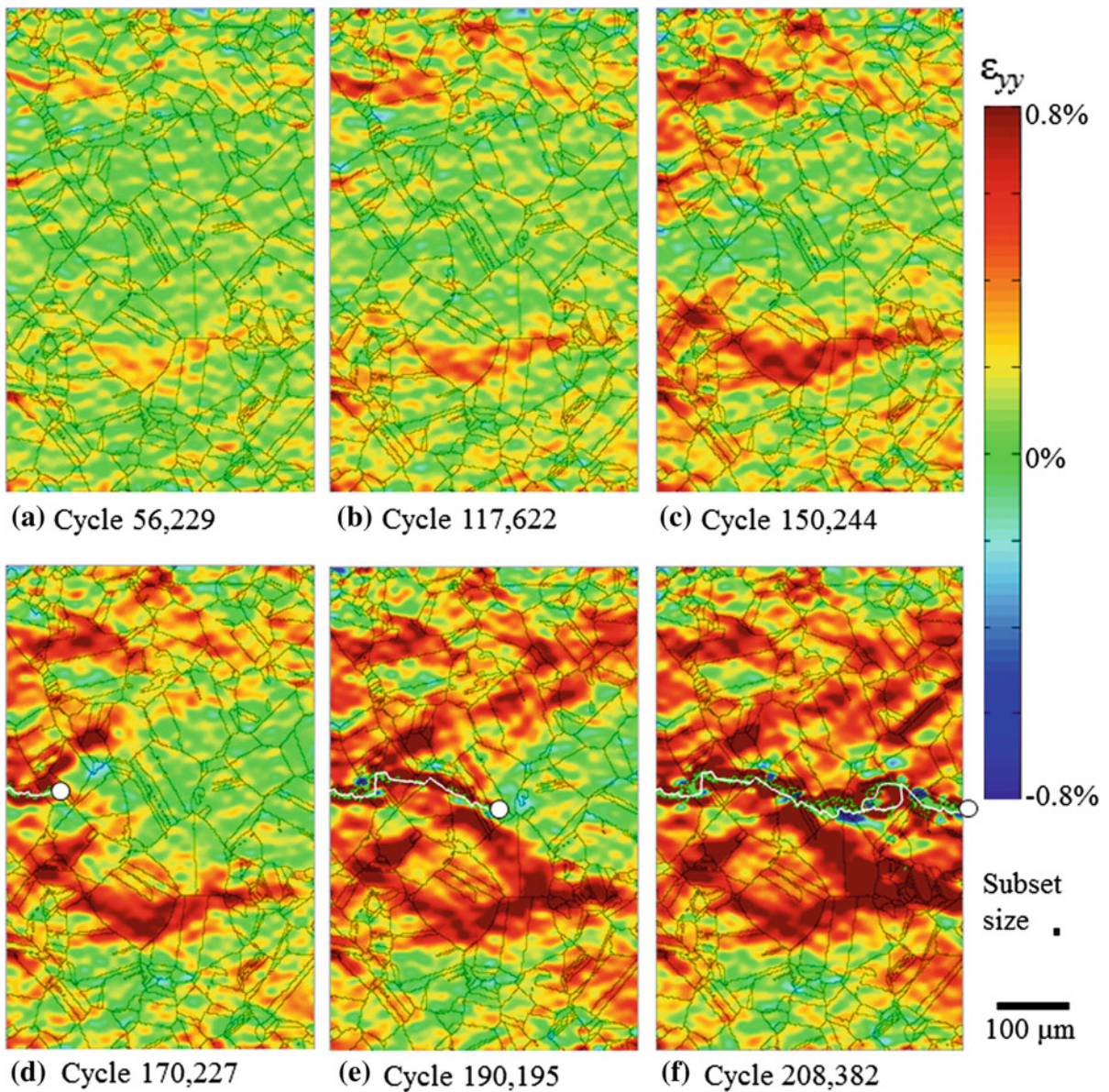


**Fig. 7** In situ plots of the strain field,  $\epsilon_{yy}$ , for region 2 at cycle numbers: **a** 56,229, **b** 117,662, **c** 150,244, **d** 170,227, **e** 190,195, and **f** 208,382. Grain boundaries are overlaid in *black*, and the

crack path is drawn in *white*. The crack does not enter this region until around cycle 160,000 although strain accumulation is measured before that time (**a–c**)

in Fig. 7 as the crack grows through region 2. The crack path is shown in white and the crack tip is illustrated by a white dot. The first three of the plots in Fig. 7a–c show that strain accumulation starts well before the crack tip enters the region indicating some fatigue damage is accumulating due to the far-field stress. The last three of these plots (Fig. 7d–f) show the strain field devel-

opment as the crack grows through the region. In these last three plots, the majority of the strain accumulation is observed to travel with the crack tip in two lobes angled approximately  $40^\circ$  ahead of the crack tip. The plot in Fig. 7e demonstrates that the extent of these lobes of plastic strain is not only far from the crack tip, but also within one grain of the crack tip. Regions

that accumulated strain well ahead of the crack tip saw strain levels intensify as the crack traveled through the region. The accuracy of the plots in Fig. 7 can be evaluated by comparing Fig. 7f to Fig. 6b. These in situ and ex situ measurements of strain are independent of one another, yet they show strain localizations in the same locations (with an obvious difference in spatial resolution).

Crack tip position can be identified in each in situ image to measure the crack length at each cycle. A plot of crack length versus cycle number as the crack grew through region 1 is shown in Fig. 8a. The slope of this plot represents the crack growth rate. A linear fit to the data (the red line) gives an average crack growth rate of 6.8 nm/cycle. Because this is constant- $K$  crack growth in the Paris regime, the crack growth rate is fairly constant. However, there are a few variations in the crack growth rate at the numbered locations. The causes for these deviations can be explained by crack path, microstructure, and strain accumulation in Fig. 8b–g. At point number 1 in Fig. 8, the crack pauses until resuming its average growth rate at point number 2. A dead end branch is observed at point 1 in Fig. 8b indicating that this crack path became less energetically favorable than a competing crack path; consequently, crack growth paused as an alternate path was formed. Figure 8d indicates that this pause at point number 1 could also be due to strain accumulation above the crack line that reduced the driving force for the crack. This strain accumulation and associated crack pause can be seen in the first video included in supplemental material. This video shows the crack length versus cycle number plot and the strain field as the crack grows through region 1. A comparison of Fig. 8d with c shows that this strain accumulation occurred within a grain containing several annealing twins (alternating orange/green in Fig. 8c). It is possible that annealing twins affect crack growth rates and local strain accumulation, but further study would be necessary to confirm or reject this hypothesis.

After the brief pause in crack growth between points 1 and 2, the crack continues to grow at the global average crack growth rate until slowing just before point 3, probably due to the deviation in crack path at that time. At point 3 (Fig. 8a), crack growth accelerates. The cause of this acceleration is not immediately clear from the image in Fig. 8e, but the series of in situ images reveals the cause. After the crack decelerates slightly at point 3, it appears to jump ahead to the point indi-

cated by the arrow in Fig. 8e. From this point, the crack appears to grow both forward and backward (to link back to point 3) simultaneously. This crack growth can be seen in the second video included in supplemental material. Of course, the crack is not truly growing backward. In reality, the subsurface crack front has grown ahead of the surface crack front (which may have also contributed to the slight deceleration before point 3). As the crack grows forward, the subsurface crack front also grows out to the surface.

After this fast surface crack growth, the crack pauses again at point 4 as it forms a crack branch (Fig. 8e). This branching pauses crack propagation until a more favorable branch forms and becomes the primary crack path (point 5 in Fig. 8). This branching is due to slip systems in local grains that provide favorable conditions for crack growth, but only on a temporary basis. The grain orientation map and in situ strain field throughout the region near the crack branching is shown in Fig. 8f, g.

Up to this point, only the  $\varepsilon_{yy}$  strain fields have been shown; however, DIC provides other components of strain as well. The three ex situ measured in-plane plastic strain components,  $\varepsilon_{yy}$ ,  $\varepsilon_{xx}$ , and  $\varepsilon_{xy}$  throughout region 1 are shown in Fig. 9a–c, respectively. From these components, the out-of-plane strain component,  $\varepsilon_{zz}$  (Fig. 9d), can be estimated by applying the assumption of incompressibility (a reasonable assumption for the high resolution DIC results since they only measure strain accumulation). By further assuming zero out-of-plane shear strain, all nine components of strain are defined and an estimate of the effective strain,  $\varepsilon_{eff}$ , can be calculated (Fig. 9e). For a true measure of the effective plastic strain, the magnitudes of the out-of-plane shear strains would need to be determined. Effective strain is often used for fatigue analysis since it incorporates all of the strain components into a scalar value. In this case, the effective strain is dominated by the axial strain component as demonstrated by the qualitative similarity of the strain plots in parts (a) and (e) of Fig. 9. The confidence interval on DIC displacements is shown in Fig. 9f. Similar to the correlation coefficient, this map gives an indication of the reliability of DIC results throughout the region. Most of the displacements within the region are accurate to within roughly 0.005 pix, but there are some regions with more uncertainty. In particular, the region immediately adjacent to the crack line has many subsets that have been thresholded (black pixels) or have uncertainties greater than

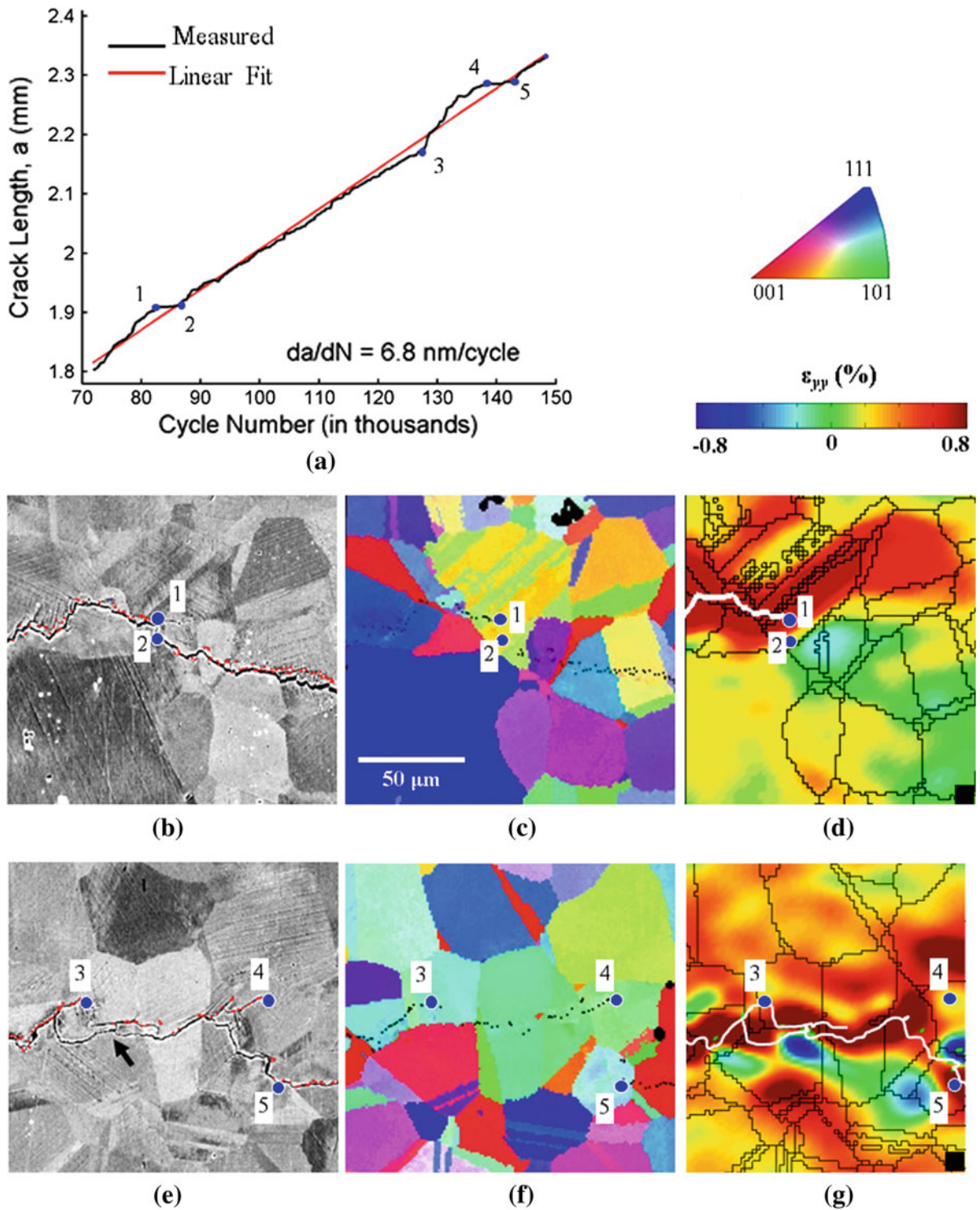


**Fig. 8** A comparison of crack growth rate, crack path, microstructure, and strain throughout region 2. **a** Crack length versus cycle number. **b** Backscatter electron image, **c** grain orientation map, **d** in situ DIC strain field  $\varepsilon_{yy}$  for the region around

points 1 and 2. **e** Backscatter electron image, **f** grain orientation map, **g** in situ DIC strain field  $\varepsilon_{yy}$  for the region around points 3–5

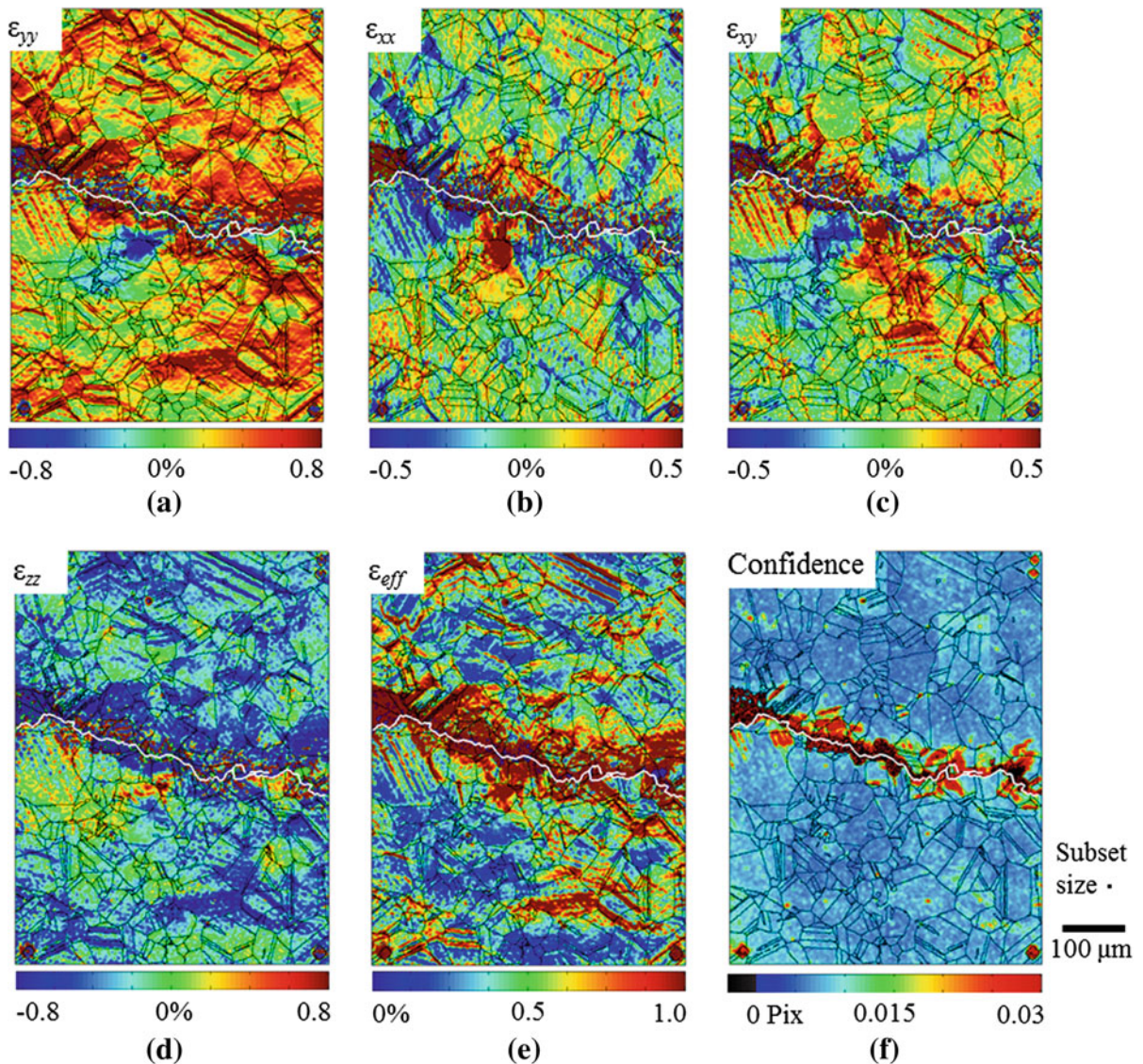


**Fig. 9** Fields obtained by DIC throughout region 1. **a**  $\epsilon_{yy}$ , **b**  $\epsilon_{xx}$ , **c**  $\epsilon_{xy}$ , **d**  $\epsilon_{zz}$  strain calculated from in-plane strains and the assumption of incompressibility, **e** Effective strain,  $\epsilon_{eff}$ , calculated from the strains in (a–d). **f** Confidence interval map show-

ing that most correlation points were accurate to within approximately 0.01 pix or less. Failed correlation points in this map are shown in *black*

0.03 pix due to crack growth through those subsets. The indentation marks also show greater uncertainty due to the lack of an adequate speckle pattern within them.

After fatigue loading and post-fatigue imaging in the scanning electron microscope, the specimen was subjected to monotonically increasing load until failure in order to view the through-thickness crack front as shown in Fig. 10. The image in Fig. 10 is the frac-

ture surface on the bottom half of the specimen. The notch can be seen on the left side and the crack front is at the right side of the image as indicated. The crack length varies throughout the specimen thickness by as much as 300  $\mu\text{m}$  although the centerline crack length is only 100  $\mu\text{m}$  further ahead than the crack length on the imaged surface. With grain sizes on the order of 90  $\mu\text{m}$  (neglecting twin boundaries), this amount of

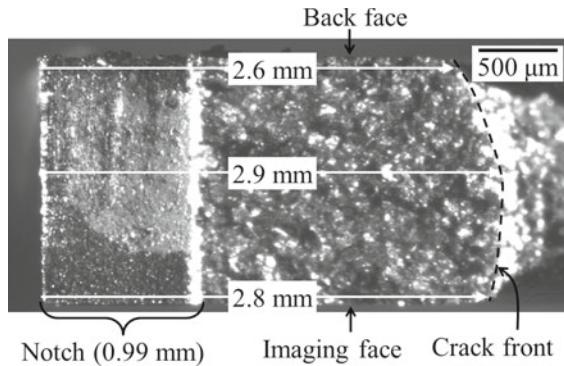


**Fig. 10** Fracture surface of the specimen (*bottom half*). The notch is on the *left* and the fatigue crack runs from the *right* end of the notch to the “crack front” line

through-thickness crack length variation is the distance of a few grain diameters.

#### 4 Discussion

Linear elastic fracture mechanics (LEFM) and the Von Mises yield criterion predict a crack tip plastic zone in a shape generally resembling a kidney bean (see the illustrated plastic zone in Fig. 5). Elastic-plastic fracture mechanics shows that the plastic zone elongates towards becoming two lobes with increasing hardening coefficient (Hutchinson 1968; Rice and Rosengren 1968; Dodds et al. 1991; Anderson 1995). The strain measurements throughout region 3 (Fig. 5) and the in situ strain measurements in Fig. 7d, e both indicate that the plastic strain travels in two lobes angled ahead of the crack tip with very little strain directly ahead of the crack tip. These lobes are pronounced and have little strain directly ahead of the crack tip, which is consistent with elastic-plastic fracture mechanics.

Although the lobes shown in this work are symmetric about the crack line, similar high-strain regions have been observed in both symmetric and asymmetric configurations in other works (McEvily and Johnston 1967; Tomkins and Biggs 1969; Neumann 1974b; Tanaka et al. 1984; Steuwer et al. 2010; Carroll et al. 2012a). These high-strain lobes are almost certainly related to the microscale slip lines associated with the blunting/sharpening mechanism of crack growth (Laird 1967), albeit at a larger scale. Examples of these microscale slip lines are visible in Fig. 4 (indicated by arrows). Several other researchers have observed these slip lines (Laird 1967; Vehoff and Neumann

1979; Peralta and Laird 1998; Peralta et al. 2007) and predicted them through models (Neumann 1974a; Davidson 1984; Peralta and Laird 1998). As with the larger-scale lobes of high-strain, microscale slip lines have appeared in both symmetric and asymmetric configurations (Laird 1967; Vehoff and Neumann 1979; Peralta and Laird 1998; Peralta et al. 2007). These two related phenomena illustrate the multiscale nature of the strain field associated with the near-crack-tip strain field in polycrystalline metals.

As the crack grows, each point experiences a changing state of stress as its position relative to the crack tip changes. However, each point at a fixed distance from the crack line experienced roughly the same history in the sense that each point had the same set of  $(r, \theta)$  positions as the crack tip approached and grew past each point. Consequently, one might expect the accumulated plastic strain in the wake of the crack to vary according to the shortest distance,  $d$ , from each point to the crack line. In Fig. 11, the effective strain at each point is plotted against its shortest distance from the actual crack path (not an assumed straight path) for each of the three regions. For all three plots, the effective strain drops off quickly with  $d$  followed by a more gradual decrease further from the crack line. Notably, there are some spikes in strain levels relatively far from the crack line. These spikes are due to the strain inhomogeneities associated with microstructure such as those shown in Fig. 6; hence, more spikes appear in regions 1 and 2, where strain measurements have sub-grain level resolution, than in region 3, in which these inhomogeneities are smoothed by the larger subset size. The presence of these spikes highlights the complex relationships between the global loading, microstructure, and strain fields.

Because LEFM predicts that strains have a  $r^{-1/2}$  dependence, with  $r$  being the distance from the crack tip, one might expect the strains behind the crack tip to have a  $d^{-1/2}$  dependence (Williams 1957). Consequently, a trend line of the form,

$$\varepsilon_{eff} = \alpha d^{-1/2}, \quad (1)$$

was fit to each set of data, with fitting parameter,  $\alpha$ . Effective strain was used because it incorporates all of the measured strain components and because it should have the same  $r^{-1/2}$  dependence as the other strain components. In regards to the data shown in Fig. 11a, b for regions 1 and 2, some correlation points gave unreasonably large strain values, although some of

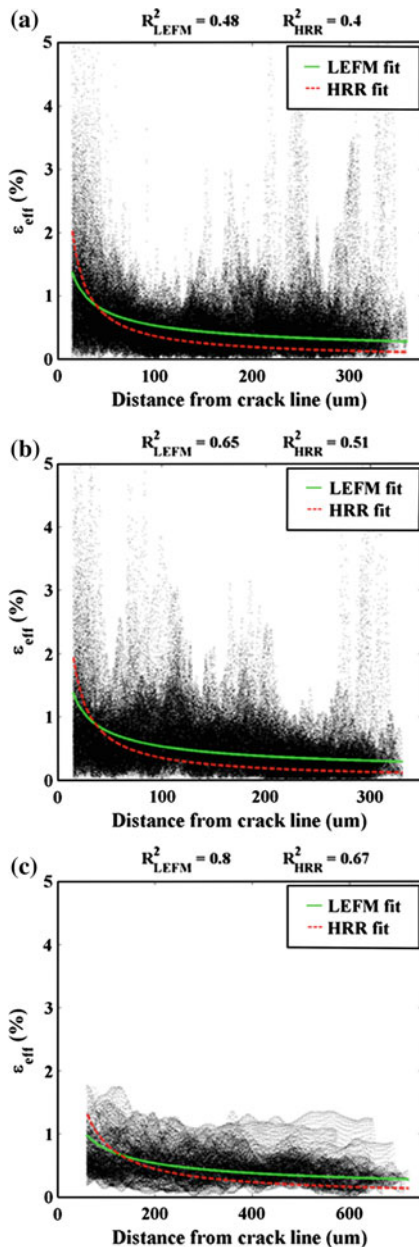


**Fig. 11** The variation of effective strain versus distance from the crack line for **a** region 1 **b** for region 2, **c** for region 3. An LEFM trend line of  $\alpha d^{-1/2}$  and an HRR trend line of  $\alpha d^{n/(n+1)}$  were fitted to the data. The coefficients of determination,  $R^2$ , for the curve fits are listed above each plot

these large strains near the crack line are real and only a subset are bad correlations. However, as it is not readily possible to separate the two, all points with effective strain above 20% were neglected in the fitting process. For region 3 (Fig. 11c), no cutoff strain was used since

the highest strains were around 20%, and only the data directly above and below the crack line were used (points ahead of the crack or behind the notch tip were neglected). Furthermore, data points that were within two subsets of the crack line (15  $\mu\text{m}$  for regions 1 and 2 and 60  $\mu\text{m}$  for region 3) were omitted from the fit. The trend line based on linear elastic fracture mechanics for each region is plotted in solid green in Fig. 11. The coefficients of determination,  $R^2$  as defined by Eisenhauer (2003), for regression through the origin, were 0.48, 0.65, and 0.80 for regions 1, 2, and 3, respectively. The LEFM curve fits appear to capture a substantial amount of the variation in strain despite the variability induced by the microstructure.

One could argue that using a trend line based on elastic-plastic fracture mechanics, such as the relation that arises from the Hutchinson, Rice, Rosengren (HRR) field (Hutchinson 1968; Rice and Rosengren 1968) would be more appropriate (Gerberich et al. 1990) since the data consists of plastic strain accumulation within the plastic zone of the crack tip. According to the HRR field, the strain field near the crack line should vary according to:

$$\varepsilon_{eff} = \alpha r^{-n/(n+1)}, \quad (2)$$

where  $n$  is the hardening exponent from the Ramberg-Osgood model as described in Hutchinson (1968). Fits to effective strain versus distance plots were performed using a hardening exponent of  $n = 10$  [a value obtained from an in-house tensile test and consistent with published values for Hastelloy X (Military Handbook 5J 2003)] and distance from the crack line,  $d$ , in the place of  $r$  in Eq. (2). These HRR trend lines, shown as dashed red lines in Fig. 11, did not fit the data quite as well as the LEFM trend lines. The  $R^2$  values for the HRR fits were 0.40, 0.51, and 0.67 for regions 1, 2, and 3, respectively.

Some of the difference between the measured strain fields and the LEFM and HRR fits is undoubtedly due to the assumptions involved in applying them to a plastic strain field behind the crack tip. Nevertheless, a considerable amount of the variability is due to microstructure as demonstrated by the large strains far from the crack line in Fig. 11. As shown in Fig. 6, the average strain in some grains is significantly higher than in others, regardless of location relative to the crack line. Furthermore, the strain within a single grain can vary significantly, and few grains deform homogeneously, which is emphasized by the slip bands and

other features in Fig. 6. The non-uniform deformation *within* grains calls into question the applicability of predicting strains through the use of orientation-based stress projection factors such as the Schmid or Taylor factor (Zhao et al. 2008; Padilla et al. 2012; Carroll et al. 2013), even if they could be applied to the complicated load history experienced by each grain in this experiment.

The local strain accumulation depends on many factors including grain shape, grain orientation, position relative to the crack line, crack path, and neighboring grains, among others. The effects of neighboring grains on the distribution of strain is significant and has been a driving force for the implementation of crystal plasticity models, which account for grain shape and orientation when modeling polycrystal deformation (Hériprié et al. 2007; Merzouki et al. 2010; Badulescu et al. 2011; Li et al. 2012; Rehr et al. 2012). In a companion effort, we have investigated a quantitative link between these microstructural features and plastic strain accumulation (Abuzaid et al. 2012a,b). In this experiment, shape and orientation of the surface grains are shown in Fig. 3. This is valuable information that can provide clues into the interaction of microstructure and local strains, but the information is incomplete since it does not contain information about the grains below the surface. It has been shown that subsurface grains can have a significant impact on surface strain fields (Hériprié et al. 2007; Zeghadi et al. 2007; Carroll et al. 2012a; Carroll et al. 2013).

Obtaining information on subsurface grain orientation for an experiment such as the one shown here would be a worthwhile endeavor. Unfortunately, three-dimensional, subsurface measurements of grain structure are expensive and time consuming. The most common techniques for obtaining three-dimensional grain orientation maps involve serial sectioning EBSD (Musienko et al. 2007; Groeber et al. 2008; Rowenhorst et al. 2010; Rowenhorst and Lewis 2011) although non-destructive techniques are in development (Herbig et al. 2011). Also affecting the surface deformation are the subsurface stress and strain fields. The development of techniques for measuring these quantities is an active area of research (Bay et al. 1999; Steuwer et al. 2010; Gates et al. 2011; Limodin et al. 2011).

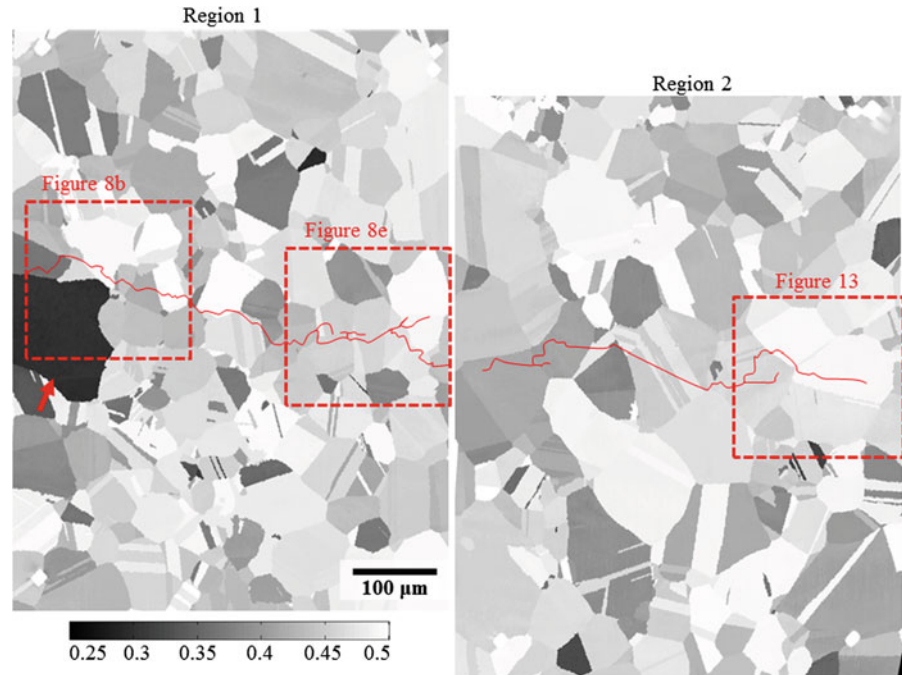
In addition to affecting the strain field, the grain structure clearly affects crack path and local crack growth rates as well. Fatigue crack growth can be

viewed as a competition between the global driving force, generally inducing a crack to grow perpendicular to the loading direction, and local microstructural resistance, which changes direction based on grain orientation. This phenomenon is illustrated in Fig. 12, which shows the Schmid factors of the grains throughout regions 1 and 2 with the assumption of vertical loading in each grain. In particular, there is a large grain at the left edge of region 1 (indicated by the arrow in Fig. 12) with a relatively small Schmid factor of 0.3 indicating it does not deform easily under vertical loading. The fact that slip in this large grain is unfavorable is likely the cause of the dramatic crack deviation just before the crack entered region 1 (see Figs. 1, 4 and 12). The crack grew around this grain following a path in which neighboring grains accommodated strain more easily. Similar, although less dramatic, effects are visible in other portions of Fig. 12. For example, the Schmid factors shown in the outlined areas within region 1 can be compared with the multiple data types shown in Fig. 8.

A slip trace analysis was performed on a grain at the right side of region 2 (outlined in Fig. 12), and the results are shown in Fig. 13. Grain orientations are shown in Fig. 13a with the crack path drawn in white. Fatigue loading was stopped such that the final crack tip position for this experiment resided within this grain. The slip trace projections from the four  $\{111\}$  slip planes are drawn on top of the backscatter electron image in Fig. 13b. The “Schmid factor” was calculated for each of the 12 face centered cubic (FCC) slip systems, four  $\{111\}$  planes each with three  $\{110\}$  directions. The maximum Schmid factor for each plane is indicated next to its slip trace. The two slip directions that appear most active have Schmid factors of 0.48 and 0.49 and slip traces that are nearly parallel to one another. The other two slip traces, with Schmid factors of 0.37 and 0.30 are closely aligned with some limited slip activity.

These Schmid factors were calculated under the assumption of unidirectional loading in the vertical direction despite the fact that the local stress field evolution is rather complicated in each grain with the stress tensor changing with crack tip position. For this grain, the slip traces with the highest calculated Schmid factors agree with the observed slip bands. Perhaps this simple unidirectional Schmid factor analysis is adequate for predicting slip in grains directly in the crack path, since although biaxial, the stress state

**Fig. 12** Schmid factors for the grains near the *crack line* in regions 1 and 2 (assuming vertical loading). In some cases, the crack travels through grains with high Schmid factors and around grains with low Schmid factors. In particular, the crack grows around the large *black* grain at the *left edge* of region 1 causing the large deviation in crack path shown in Fig. 1. Areas that are shown in other figures are outlined by *rectangles* for comparison



directly at the crack tip is likely dominated by opening stress. However, it is doubtful that this simple analysis would be accurate for grains further from the crack path or in other regions of increased biaxiality. A rigorous analysis of fatigue crack growth with Schmid factors that consider multiaxial loading would be extremely useful, but is beyond the scope of the present effort.

The crack path within the grain analyzed in Fig. 13b frequently follows the dominant slip direction. However, the angle of the crack path is shallower than the angle of the slip traces because the crack path does not follow a single slip system. Instead, the crack appears to grow along one slip system for a short distance before jumping to another, parallel slip system. These jogs between parallel slip systems are a result of crack growth along the secondary slip systems as has been observed by other researchers (Neumann 1969). The crack also appears to follow crystallographically favorable slip planes in Fig. 8 (just before point 1) and at the locations indicated by arrows in Fig. 4. This is consistent with a three-dimensional comparison of a crack surface with crystallographic planes by Herbig et al. (2011). When looking at the fracture surface, those researchers found very few grains in which the fracture surface was along a single crystallographic direction. The fracture planes in most grains either alternated

between two planes or had a complicated mixture of several planes.

From the analyses shown in this work, particularly in Fig. 8, it appears that the favorable crystallographic slip planes may increase the local crack growth rate. As was shown in Fig. 8 at points 1 and 4, a favorable slip direction within a grain may only be favorable for a short period of time. This can lead to crack branching, which subsequently slows crack growth. Additionally, point 1 in Fig. 8 indicates that twins may play a role in temporarily slowing crack growth by inducing strain localizations that lessen the driving force for crack growth. This work revealed some of the causes of local deviations in crack growth rate, but it is important note that the overall crack growth rate in region 1 appeared to be relatively unaffected by these deviations (Fig. 8a). This is an expected consequence of constant-K loading in the Paris regime of fatigue crack growth. In a similar vein, this crack is long compared to the microstructure so that the crack path is expected to be straight according to Forsyth's stage II crack growth characterization (Forsyth 1963). Nevertheless, some variation in the crack path is observed. Because this variation is only about 100  $\mu\text{m}$  at most, approximately one grain diameter (Figs. 5 and 6), the crack can be considered to be growing straight in a global sense even while it exhibits this local tortuosity.

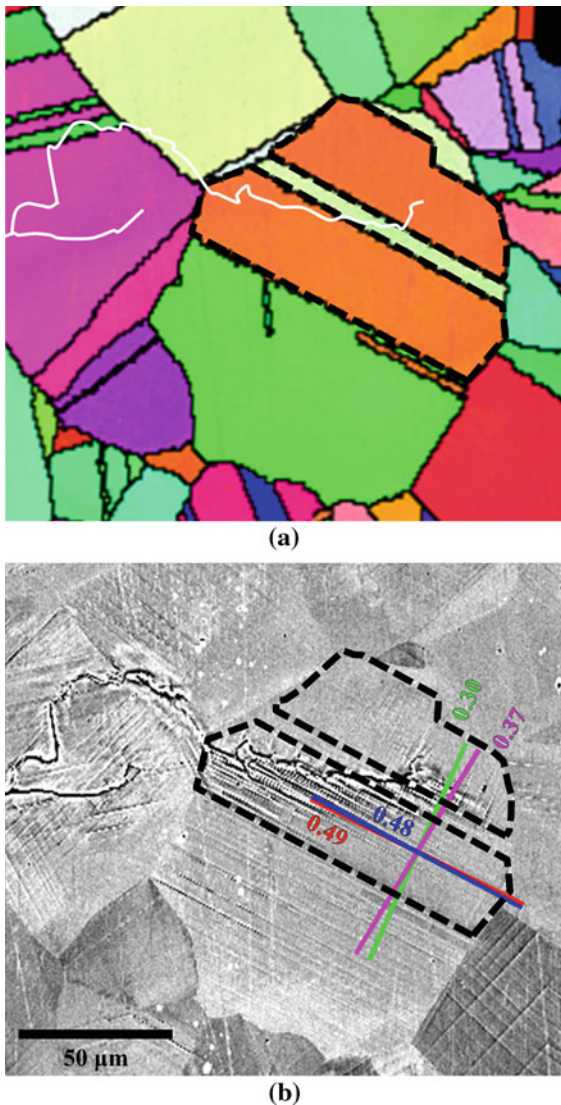


**Fig. 13** **a** Grain orientation map (with respect to the loading axis) in the region near the final crack tip position as shown in Fig. 12. **b** Backscatter electron image of the region shown in (a). Slip traces and associated Schmid factors are calculated from the grain orientation information shown in (a). The crack appears to follow *slip lines* in this grain, but not exclusively; instead, the crack appears to form on multiple *slip lines* with small jogs between crack sections

## 5 Conclusions

Combined ex situ and in situ DIC techniques provided measurements of the strain field near a growing fatigue crack with sub-grain level resolution. The in situ measurements also showed how these strains developed over time with crack propagation. The plastic strain

field traveled in two lobes angled ahead of the crack tip with almost no strain accumulation directly ahead of the crack. A considerable amount of inhomogeneity, which was strongly influenced by microstructure, was observed in the plastic wake behind the crack tip.

This work examined the local relationships between four variables in fatigue crack growth: crack path, microstructure, crack growth rate, and strain field. The following relationships were observed:

- The local crack growth rate is affected by the local strain field, crack path, and microstructure. Local strain accumulation can reduce the crack growth driving force, branches and tortuosity in the crack path can slow crack growth, and grain orientation can favor faster or slower local crack growth rates. The long-term crack growth rate over many cycles represents an average of many of these factors, sometimes competing.
- The strain field within the crack tip plastic region is influenced by both location relative to the crack path and microstructure. The effective strain generally decreased with distance from the crack line in proportion to  $d^{-1/2}$  as predicted by linear elastic fracture mechanics. Predictions from the HRR field did not agree as well with the data. Differences between predictions could be due to the assumptions necessary to compare these models to plastic strain fields behind the crack tip, but the influential role of microstructure was evident.
- The local crack path was shown to depend on microstructure. In particular, the crack deviated significantly in order to go around a large grain that was unfavorably oriented for slip (i.e., had a low Schmid factor). Microscale slip lines at the crack tip are determined largely by local grain orientation and influence the crack growth direction. However, crack growth was rarely along a single slip plane within a grain; it alternated between multiple slip planes and sometimes appeared to grow in directions not associated with any obvious slip plane. The favorability of crystallographic slip planes may also affect local crack growth rates, but not in a straightforward manner.
- The strain field was shown to have some effect on crack path and crack growth rate. In one instance, strain accumulation in a twinned region may have contributed to retardation of the crack growth rate.

In contrast, strains associated with crystallographic slip may create conditions favorable for faster crack growth and may influence crack path.

There are numerous relationships among the many variables associated with fatigue crack growth. This work has elucidated a few of these relationships by comparing multiple sets of data on a growing fatigue crack. As demonstrated in this work, microstructure and local strains both play an important role in fatigue crack growth behavior.

**Acknowledgments** This work was supported by the Midwest Structural Sciences Center (MSSC), which is sponsored by the Air Vehicles Directorate of the U.S. Air Force Research Laboratory under contract number FA8650-06-2-3620. The guidance and support of Dr. Ravi Chona at the Air Force Research Laboratory is greatly appreciated. Sandia National Laboratories is a multi-program laboratory managed and operated by Sandia Corporation, a wholly owned subsidiary of Lockheed Martin Corporation, for the U.S. Department of Energy's National Nuclear Security Administration under contract DE-AC04-94AL85000.

## References

- Abuzaid WZ, Sangid MD, Carroll JD, Sehitoglu H, Lambros J (2012a) Slip transfer and plastic strain accumulation across grain boundaries in Hastelloy X. *J Mech Phys Solids* 60: 1201–1220
- Abuzaid WZ, Sehitoglu H, Lambros J (2012b) Plastic strain localization and fatigue micro-crack formation in Hastelloy X. *Mater Sci Eng A (Structural Materials: Properties, Microstructure and Processing)* (in press)
- Anderson TL (1995) *Fracture mechanics, fundamentals and applications*, 2nd edn. CRC Press, Inc., Boca Raton, FL
- Badulescu C, Grediac M, Haddadi H, Mathias JD, Balandraud X, Tran HS (2011) Applying the grid method and infrared thermography to investigate plastic deformation in aluminium polycrystal. *Mech Mater* 43:36–53
- Barker DB, Sanford RJ, Chona R (1985) Determining K and related stress-field parameters from displacement-fields. *Exp Mech* 25:399–407
- Bay BK, Smith TS, Fyhrie DP, Saad M (1999) Digital volume correlation: three-dimensional strain mapping using X-ray tomography. *Exp Mech* 39:217–226
- Carroll J, Abuzaid W, Lambros J, Sehitoglu H (2010) An experimental methodology to relate local strain to microstructural texture. *Rev Sci Instrum* 81:083703
- Carroll J, Efstathiou C, Lambros J, Sehitoglu H, Hauber B, Spottswood S, Chona R (2009) Investigation of fatigue crack closure using multiscale image correlation experiments. *Eng Fract Mech* 76:2384–2398
- Carroll JD, Abuzaid W, Lambros J, Sehitoglu H (2012a) High resolution digital image correlation measurements of strain accumulation in fatigue crack growth. *Int J Fatigue*. doi:10.1016/j.ijfatigue.2012.06.010
- Carroll JD, Brewer LN, Battaile CC, Boyce BL, Emery JM (2012b) The effect of grain size on local deformation near a void-like stress concentration. *Int J Plast* 39:46–60
- Carroll JD, Clark BG, Buchheit TE, Michael JR, Boyce BL (2013) An experimental analysis of stress projection factors in BCC Tantalum (in preparation)
- Davidson DL (1984) A model for fatigue crack advance based on crack tip metallurgical and mechanics parameters. *Acta Metall* 32:707–714
- Delaire F, Raphanel JL, Rey C (2000) Plastic heterogeneities of a copper polycrystal deformed in uniaxial tension: experimental study and finite element simulations. *Acta Mater* 48: 1075
- Dodds RH, Anderson TL, Kirk MT (1991) A framework to correlate a/W ratio effects on elastic-plastic fracture-toughness (Jc). *Int J Fract* 48:1–22
- Efstathiou C, Sehitoglu H, Lambros J (2010) Multiscale strain measurements of plastically deforming polycrystalline titanium: role of deformation heterogeneities. *Int J Plast* 26:93
- Eftis J, Subramonian N, Liebowitz H (1977) Crack border stress and displacement equations revisited. *Eng Fract Mech* 9:189–210
- Eisenhauer JG (2003) Regression through the origin. *Teach Stat* 25:76–80
- El Bartali A, Aubin V, Degallaix S (2009) Surface observation and measurement techniques to study the fatigue damage micromechanisms in a duplex stainless steel. *Int J Fatigue* 31:2049–2055
- Elber W (1970) Fatigue crack closure under cyclic tension. *Eng Fract Mech* 2:37–45
- Elber W (1971) The significance of fatigue crack closure. *Damage Toler Aircr Struct ASTM STP* 486:230–242
- Forsyth PJE (1963) Fatigue damage and crack growth in aluminum alloys. *Acta Metall* 11:703–715
- Gates M, Lambros J, Heath MT (2011) Towards high performance digital volume correlation. *Exp Mech* 51:491–507
- Gerberich WW, Davidson DL, Kaczorowski M (1990) Experimental and theoretical strain distributions for stationary and growing cracks. *J Mech Phys Solids* 38:87–113
- Groeber M, Ghosh S, Uchic MD, Dimiduk DM (2008) A framework for automated analysis and simulation of 3D polycrystalline micro structures. Part 1: statistical characterization. *Acta Mater* 56:1257–1273
- Herbig M, King A, Reischig P, Proudhon H, Lauridsen EM, Marrow J, Buffiere J-Y, Ludwig W (2011) 3-D growth of a short fatigue crack within a polycrystalline microstructure studied using combined diffraction and phase-contrast X-ray tomography. *Acta Mater* 59:590–601
- Héripin E, Dexet M, Crépin J, Gélébart L, Roos A, Bornert M, Caldemaison D (2007) Coupling between experimental measurements and polycrystal finite element calculations for micromechanical study of metallic materials. *Int J Plast* 23:1512
- Hutchinson JW (1968) Singular behaviour at end of a tensile crack in a hardening material. *J Mech Phys Solids* 16: 13–31
- Kmieciak KJ (1994) Determination of the fracture parameters associated with mixed mode displacement fields and applications of high density geometric Moiré. Texas A&M University, College Station

- Kobayashi AS, Harris DO, Engstrom WL (1967) Transient analysis in a fracturing magnesium plate. *Exp Mech* 7:434–440
- Laird C (1967) Influence of metallurgical structure on the mechanisms of fatigue crack propagation. *Fatigue Crack Propag ASTM-STP* 415:131–180
- Laird C, Smith GC (1963) Initial stages of damage in high stress fatigue in some pure metals. *Phil Mag* 8:1945–1963
- Lankford J (1985) The influence of microstructure on the growth of small fatigue cracks. *Fatigue Fract Eng Mater Struct* 8:161–175
- Li CS, Orlecky LJ (1993) Fiducial grid for measuring microdeformation ahead of fatigue-crack tip near aluminum bicrystal interface. *Exp Mech* 33:286–292
- Li Y, Aubin V, Rey C, Bompard P (2012) Polycrystalline numerical simulation of variable amplitude loading effects on cyclic plasticity and microcrack initiation in austenitic steel 304L. *Int J Fatigue* 42:71–81
- Limodin N, Rethore J, Buffiere J-Y, Hild F, Ludwig W, Rannou J, Roux S (2011) 3D X-ray microtomography volume correlation to study fatigue crack growth. *Adv Eng Mater* 13:186–193
- Littlewood PD, Wilkinson AJ (2012) Local deformation patterns in Ti-6Al-4V under tensile, fatigue and dwell fatigue loading. *Int J Fatigue* 43:111–119
- Liu HW, Ke JS (1975) Moire method. In: Kobayashi AS (ed) *Experimental techniques in fracture mechanics, II, SEM monograph, No 2*. The Iowa State University Press, Ames, IA, pp 111–165
- Luo PF, Chao YJ, Sutton MA, Peters WH (1993) Accurate measurement of 3-dimensional deformations in deformable and rigid bodies using computer vision. *Exp. Mech* 33:123–132
- McEvily AJ, Boettner RC (1963) On fatigue crack propagation in FCC metals. *Acta Metall* 11:725–743
- McEvily AJ, Johnston TL (1967) Role of cross-slip in brittle fracture and fatigue. *Int J Fract Mech* 3:45–74
- McNeill SR, Peters WH, Sutton MA (1987) Estimation of stress intensity factor by digital image correlation. *Eng Fract Mech* 28:101–112
- Merzouki T, Collard C, Bourgeois N, Meraghni F (2010) Coupling between measured kinematic fields and multicrystal SMA finite element calculations. *Mech Mater* 42:72
- Military Handbook 5J (2003) *Metallic materials and elements for aerospace vehicle structures Section 6.3.1: Hastelloy X*. U.S. Department of Defense
- Musienko A, Tatschl A, Schmidegg K, Kolednik O, Pippan R, Cailletaud G (2007) Three-dimensional finite element simulation of a polycrystalline copper specimen. *Acta Mater* 55:4121–4136
- Neumann P (1969) Coarse slip model of fatigue. *Acta Metall* 17:1219–1225
- Neumann P (1974a) Geometry of slip processes at a propagating fatigue crack 2. *Acta Metall* 22:1167–1178
- Neumann P (1974b) New experiments concerning slip processes at propagating fatigue cracks 1. *Acta Metall* 22:1155–1165
- Nicoletto G, Post D, Smith CW (1982) Moire interferometry for high sensitivity measurements in fracture mechanics. *SESA/JSME Jt Conf Exp Mech, Oahu-Maui, HI*
- Padilla HA, Lambros J, Beaudoin AJ, Robertson IM (2012) Relating inhomogeneous deformation to local texture in zirconium through grain-scale digital image correlation strain mapping experiments. *Int J Solids Struct* 49:18–31
- Paris P, Erdogan F (1963) Critical analysis of crack propagation laws. *Am Soc Mech Eng Trans J Basic Eng* 85:528–534
- Peralta P, Choi SH, Gee J (2007) Experimental quantification of the plastic blunting process for stage II fatigue crack growth in one-phase metallic materials. *Int J Plast* 23:1763–1795
- Peralta P, Laird C (1998) Fatigue fracture at bicrystal interfaces: experiment and theory. *Acta Mater* 46:2001–2020
- Rehrl C, Kleber S, Antretter T, Pippan R (2011) A methodology to study crystal plasticity inside a compression test sample based on image correlation and EBSD. *Mater Charact* 62:793–800
- Rehrl C, Voelker B, Kleber S, Antretter T, Pippan R (2012) Crystal orientation changes: a comparison between a crystal plasticity finite element study and experimental results. *Acta Mater* 60:2379–2386
- Rice JR, Rosengren GF (1968) Plane strain deformation near a crack tip in a power-law hardening material. *J Mech Phys Solids* 16:1–12
- Ritchie RO (1999) Mechanisms of fatigue-crack propagation in ductile and brittle solids. *Int J Fract* 100:55–83
- Roux S, Rethore J, Hild F (2009) Digital image correlation and fracture: an advanced technique for estimating stress intensity factors of 2D and 3D cracks. *J Phys D Appl Phys* 42:214004
- Rowenhorst DJ, Lewis AC (2011) Image processing and analysis of 3-D microscopy data. *Jom* 63:53–57
- Rowenhorst DJ, Lewis AC, Spanos G (2010) Three-dimensional analysis of grain topology and interface curvature in a beta-titanium alloy. *Acta Mater* 58:5511–5519
- Sanford RJ (1989) Determining fracture parameters with full-field optical methods. *Exp Mech* 29:241–247
- Sanford RJ, Dally JW (1979) General-method for determining mixed-mode stress intensity factors from isochromatic fringe patterns. *Eng Fract Mech* 11:621–633
- Sharpe Jr WN (1982) *Coherent optical methods of stress-intensity factor measurement*. SESA/JSME Jt Conf Exp Mech. Oahu-Maui, HI
- Steuwer A, Rahman M, Shterenlikht A, Fitzpatrick ME, Edwards L, Withers PJ (2010) The evolution of crack-tip stresses during a fatigue overload event. *Acta Mater* 58:4039–4052
- Suresh S, Ritchie RO (1984) Propagation of short fatigue cracks. *Int Met Rev* 29:445–476
- Tanaka K, Hoshida T, Sakai N (1984) Mechanics of fatigue crack propagation by crack-tip plastic blunting. *Eng Fract Mech* 19:805–825
- Tomkins B, Biggs WD (1969) Low endurance fatigue in metals and polymers, Part 3: mechanisms of failure. *J Mater Sci* 4:544–553
- Tschopp MA, Bartha BB, Porter WJ, Murray PT, Fairchild SB (2009) Microstructure-dependent local strain behavior in polycrystals through in-situ scanning electron microscope tensile experiments. *Metall Mater Trans A* 40:2363
- Vehoff H, Neumann P (1979) In situ SEM experiments concerning the mechanism of ductile crack growth. *Acta Metall* 27:915–920
- Williams DR, Davidson DL, Lankford J (1980) Fatigue crack tip plastic strains by the stereomicroscopy technique. *Exp Mech* 20:134–139
- Williams ML (1957) On the stress distribution at the base of a stationary crack. *J Appl Mech* 24:109–114

- Zeghadi A, Forest S, Gourgues AF, Bouaziz O (2007) Ensemble averaging stress-strain fields in polycrystalline aggregates with a constrained surface microstructure-Part 2: crystal plasticity. *Phil Mag* 87:1425–1446
- Zhang N, Tong W (2004) An experimental study on grain deformation and interactions in an Al-0.5%Mg multicrystal. *Int J Plast* 20:523–542
- Zhao Z, Ramesh M, Raabe D, Cuitino AM, Radovitzky R (2008) Investigation of three-dimensional aspects of grain-scale plastic surface deformation of an aluminum oligocrystal. *Int J Plast* 24:2278